Responsible Federal Agency:	Department of Energy, Energy Efficiency and Renewable Energy, Solid State Lighting Program
FOA:	DE-FOA-0002196
Report:	Final Technical Report
Award Number:	DE-EE0009692
Award Type:	Grant
Prime Recipient:	OSRAM Opto-Semiconductors 9025 NE Von Neumann Drive, Suite 120 Hillsboro, OR 97006 USA
Prime Recipient Type:	For Profit Business
Prime Recipient's DUNS number:	809525582
Project Title:	Cadmium-Free QD Building Blocks for Human Centric Lighting
Principle Investigators:	David O'Brien, OSRAM Opto-Semiconductors, David.OBrien@ams-osram.com Jonathan Owen, Columbia University Emory Chan, Lawrence Berkeley National Lab
Submitting Official:	Melody Kessler, OSRAM Opto-Semiconductors, Melody.Kessler@ams-osram.com
Project Dates:	10/1/2021–3/31/2024
Date of Report:	7/2024

This material is based upon work supported by the U.S. Department of Energy's Office of Energy Efficiency and Renewable Energy (EERE) under the Building Technologies Office Solid State Lighting R&D Opportunities award number DE-EE0009692.

I. Executive Summary

This project developed Cd-free quantum dot (QD) downconverters for efficacious human-centric lighting (HCL) light emitting diode (LED) devices. Solid state HCL devices address the lack of light in the cyan wavelength region (460-490 nm) in white LEDs by enhancing the melanopic daylight efficacy ratio (MDER) value. MDER is a metric that indicates the degree to which artificial lighting stimulates nonvisual biological processes in the retina responsible for regulating circadian rhythms compared with natural lighting. The peak sensitivity of melanopsin in the retina is at 479 nm, therefore artificial lighting which can fill the well-known "cyan gap" may improve human health. Due to the Restriction of Hazardous Substances (RoHS) regulations, cadmium-free core/shell/shell QDs are the primary targets for low toxicity, tunable downconverters.

Cyan- and red-emitting core/shell/shell QDs were implemented in LED devices toward achieving a brightness of 210 lm/W at 4000 K, CRI 90, and MDER > 0.7. Synthetic development of Cd-free materials yielded cyan InP/ZnS QDs with a photoluminescence quantum yield (PLQY) of ~60% between 480-490 nm, and red InP/ZnSe/(ZnSeS)/ZnS QDs reaching ~80% PLQY at 620-630 nm. We successfully demonstrated that the inclusion of cyan QDs increased the MDER value to ≥0.7, but the brightness of the HCL LED devices was hindered due to low PLQY values. However, upon substitution of the Cd-free cyan QD with a low-Cd QD with >90% PLQY, brightness improved by 25% over the Cd-free device to 179 lm/W. Despite the technical obstacles remaining toward improving emission characteristics and stability of QDs under high flux, we have confirmed the promise of narrow, tunable QD emitters in SSL packages toward the goal of healthy, human-centric lighting.

II. Accomplishments

IIA. Summary of Project Activities

The project targeted the synthesis of III-V/II-VI QDs emitting near 475 nm and 620 nm with high photoluminescence quantum yield (PLQY) values of >85% and full width at half maximum (FWHM) values of <40 nm (Task 1). Task 2 aimed to improve upon the brightness and stability of the QD materials through surface ligation and semiconductor facet control. Task 3 investigated the application of novel and proprietary chemical barriers, as well as reliability testing of QDs on-chip under High Temperature Operating Lifetime (HTOL) and Wet-HTOL (WHTOL) conditions, and in film under high flux and temperature. Lastly, Task 4 determined the optimal LED pump wavelength, which was used to demonstrate full-spectrum and CRI 90 cyan-enhanced LEDs. The goal of the project was to achieve a CRI 90 device at 4000 K and an MDER of > 0.7 with high brightness, striving toward 210 lm/W.

IIB. Significant Achievements

1) Demonstrated a Cd-free LED with a performance of 142 lm/W at 4000 K, CRI >90, MDER = 0.7.
2) Determined the major loss pathway of the Cd-free device was double pumping of phosphors and red QDs with cyan QDs. Using a low-Cd ZnCdSSe cyan QD with PLQY of >90%, the final device brightness increased to 179 lm/W, a result competitive with two-chip and HCL solutions currently on the market.

3) Investigated fluorination mechanisms on InP QDs and InP/ZnS QDs to achieve PLQY values of ~82% for both systems[1]
4) Developed high-throughput robotic screening for optimization of fluorination chemistry on InP/ZnS, achieving enhancements of >35% over earlier reports.
5) Achieved the successful synthesis of crystalline GaP, a material proposed to improve QD absorption, through novel reaction pathways.
6) Deposited thick ZnS shells with high resilience toward flux-induced degradation. QDs with thick ZnS shells enabled downstream study of stability during barrier deposition and porous glass infusion.

[1] Valleix, R., Zhang, W., Jordan, A., Guillemeney, L., Castro, L., Zekarias, B., Park, S., Wang, O., Owen, J. *Nano Lett*. **2024**, *24*, 5722−5728

IIC. Outcomes of Project Objectives

MILESTONE SUMMARY FOR BUDGET PERIOD 1				
Milestone Number	**Milestone**	**Planned Completion Date**	**Verification Method**	**Outcome**
M1.1.1	ZnCdSSe/ZnS (cyan) 1 g, 475 ± 15 nm, FWHM < 35 nm emitter, PLQY > 90%	3/31/22	Standardized optical testing protocol. X-ray diffraction. TEM.	Did not achieve 1g scale, PLQY ~75%
M4.1.1	Determine proper LED light source Demonstrate cyan-enhanced white light LED with ZnCdSSe/ZnS QD and establish baseline HCL values	3/31/22	Computer modelling parameterized with empirical results from test device builds	123 lm/W
M4.1.2	Determine optimal LED pump wavelength	6/30/22	Consider cost and long-term potential of LED source verses efficacy and color quality of white solution	450 nm
M1.2.1	InGaP/GaP/Zn(Se)S/ZnS (cyan) 0.1 g, 475 ± 15 nm, FWHM < 40 nm, PLQY > 85%	9/30/22	Standardized optical testing protocol. X-ray diffraction. TEM.	PLQY ~60%
M1.3.1	InGaP/GaP/Zn(Se)S/ZnS (red) 1 g, 620 ± 15 nm, FWHM < 40 nm, PLQY > 85%	12/31/22	Standardized optical testing protocol. X-ray diffraction. TEM.	FWHM ~50 nm, PLQY ~80%
M2.1.1	Facet Control During InGaP/(ZnSe)/ZnS core-shell Synthesis	12/31/22	Successful initial HERMAN screening run w/ Zn salts	Facet control achieved; benefit not shown
M2.3.1	Demonstrate and quantify PLQY stability InGaP/GaP/ZnS QDs Solution/shelf stability- PLQY retention as a function of challenge condition, eg. pH	12/31/22	Relative brightness and color stability measured by standardized optical testing protocol as a function of challenge condition	Developed chemical and flux challenges
M4.1.3	Tune QD size, composition for high absorption	12/31/22	(ODoptimal / ODpeak) > 4	Amorphous GaP increased Abs, no PL
M4.3.1	Demonstrate cyan-enhanced capability of Cd-free QDs	12/31/22	CRI Ra = 90, CCT = 4000, MDER (D65) > 0.7	Demonstrated
Go/No-Go	Demonstrate cyan-enhanced capability of Cd-free QDs	12/31/22	CRI Ra = 90, CCT = 4000, MDER (D65) > 0.7, 160 lm/W, solution PLQY > 60% for cyan and red QDs	139 lm/W achieved at target metrics

MILESTONE SUMMARY FOR BUDGET PERIOD 2				
Milestone Number	**Milestone**	**Planned Completion Date**	**Verification Method**	**Outcome**
M3.1.1	Optimize chemical bath deposition of hydroxyapatite onto InGaP/ZnS QDs to establish baseline PLQY. Grow >5 nm of hydroxyapatite onto QDs	3/31/23	Standardized optical testing protocol. X-ray diffraction. TEM.	Exceeded 5 nm, PLQY retention 63%
M3.3.1	Novel barrier coated Cd-Free QD system with a PLQY > 50 % Measured in film at 10W/cm^2, 120 °C	6/30/23	Standardized optical testing protocol.	PLQY = 30% in film
M4.2.1	Barrier-coated QD Stability Studies: PLQY Maintenance > 50% of baseline at 500 hrs LED HTOL & WHTOL Reliability	6/30/23	Real time monitoring of changes in efficacy and color metrics in test LED devices under industry-standardized conditions	PLQY = 40% at t=0
DP1	Report best surface chemistry for novel barrier coating	6/30/23	Comparison of optical brightness and reliability for candidate processes	DDT
DP2	Opt to pursue porous glass encapsulation based on PLQY and reliability data	6/30/23	Comparison of optical brightness and reliability for candidate processes	QDs incorporated into porous glass; not concentrated enough for chip
M3.2.1	Demonstrate next gen capabilities of metal-oxide encapsulation of QDs HTOL and WHTOL 1000-hour reliability challenges by 50% over manufacturing baseline methods.	9/30/23	Real time monitoring of changes in efficacy and color metrics in test LED devices under industry-standardized conditions	Pushed to Q8
M3.3.2	Novel barrier coated Cd-Free QD system with a PLQY > 90% Measured in film at 10W/cm^2, 120 °C	9/30/23	Standardized optical testing protocol.	PLQY still 30% in film
M4.2.2	Barrier-coated QD Stability Studies: PLQY Maintenance > 100% of baseline at 1000 hrs LED HTOL & WHTOL Reliability	12/31/23	Real time monitoring of changes in efficacy and color metrics in test LED devices under industry-standardized conditions	QDs stable under storage conditions, not under high flux
M4.3.2	Demonstrate full spectrum capability by building LEDs with Cd-free of PLQY > 90% for red and cyan QDs	12/31/23	CRI Ra = 95, CCT = 4000, MDER (D65) > 0.7	Done
M4.3.3	Demonstrate CRI 90, 4000K device with red, Cd-free QDs	12/31/23	CRI Ra = 90, CCT = 4000, MDER (D65) > 0.7, 210 lm/W	142 lm/W with Cd-free; 179 lm/W with low-Cd cyan

III. Detailed Project Accomplishments
IIIA. Synthesis of HCL-focused downconverters
IIIA.1 ZnCdSSe QDs for cyan emission

Toward obtaining bright and narrow Cd-free cyan and red emitters, we worked on developing cyan-emitting ZnCdSSe/ZnS core/shell nanocrystals as a model system for the targeted In(Ga)P/ZnSe/ZnS core/shell structures (Subtask 1.1). Following work from previously developed ZnCdSSe/ZnS core/shell nanocrystal synthetic strategies developed at Columbia in conjunction with the Molecular Foundry, shelling conditions were optimized for large scale synthesis. Benzyl thiols were found to provide an inexpensive, commercially available route to drastically improve the PLQY of ZnCdSSe cores from >100mM concentrations of ZnS precursor solution (**Figure 1**).

Since Milestone 1.1.1 specifies the synthesis of 1 g of ZnCdSSe/ZnS, the reaction concentration was increased by 3× to 20.3 mM from the optimized reaction conditions. An increase in the reaction concentration yielded 733 mg of ZnCdSSe/ZnS with an excitonic absorption feature of 458 nm, emission maximum of 484 nm, and FWHM of 45 nm. The reaction concentration was slightly lowered to 16.3 mM to study the effect of reaction concentration on the absorption and emission linewidth of ZnCdSSe/ZnS. Surprisingly, lowering the concentration led to red-shifting of the excitonic absorption feature to 472 nm and the emission maximum to 490 nm, as well as increasing the FWHM to 52 nm. Likely, a change in the reaction concentration impacts the relative conversions of Zn and Cd; a redshift could indicate higher Cd incorporation, decreasing the band gap.

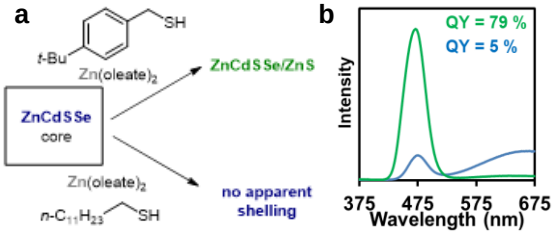

Figure 1. a) Scheme for the shelling of ZnCdSSe nanocrystal cores from various thiols. b) Photoluminescence spectra comparison of ZnS shelling using alkyl and benzyl thiols.

Though we did not scale the synthesis of this material to 1 g at the desired specifications, high-quality ZnCdSSe/ZnS QDs were obtained at a ~200 mg scale. These QDs were utilized throughout the two-year project to demonstrate the promise of high-PLQY cyan emitters within an HCL LED device. Moreover, the shelf stability of the material is remarkable, maintaining near-unity PLQY after years stored under ambient conditions.

IIIA.2 Cd-free QDs for cyan emission

The synthesis of small InP QDs emitting in the cyan region was a challenging yet crucial task to obtaining a cyan-enhanced HCL device. Researchers at Columbia and OSRAM explored synthetic routes toward InP via two common phosphorus precursors: tris(trimethylsilyl) phosphine and tris(diethylamino) phosphine. Equally important, the subsequent zinc chalcogenide shells dictate color, PLQY, and stability of the core/shell heterostructures. Early in the project, we demonstrated that thicker ZnS shells improve PLQY (**Figure 2**). After further development, we

concluded that samples with the best performance for LEDs did not contain a ZnSeS shell; rather, two ZnS shells conferred the optimal combination of PLQY and centroid.

The results in **Figure 3** demonstrate that 475 nm emission is difficult to obtain. Wavelength is especially important when implementing QDs on chip; at high QD loads, the spectrum red-shifts compared with dilute solution measurements due to self-absorption. Working together, we have explored a large parameter space and selected a cyan-emitting QD sample that contributes to the MDER > 0.7 on device. The bluest and brightest samples were InP/ZnS/ZnS, and were ultimately selected for use in the Go/No-Go and Final devices, with reproducible PLQY values of 63-68%, centroids at 478-488 nm, and FWHM values of 47-49 nm.

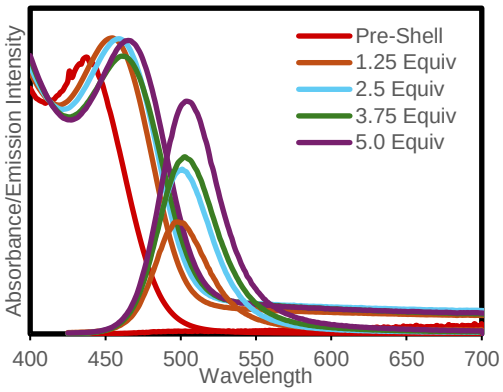

Figure 2. Zinc sulfide shelling reaction of an InP core utilizing 4-tertbutyl benzyl mercaptan. Absorbance and emission intensity of the InP/ZnS core/shell structures by equivalents of sulfur precursor added.

While the centroid and FWHM values are satisfactory, the obstacle remaining for cyan-emitting QDs in LED devices is PLQY. One significant barrier to achieving a high PLQY for a Cd-free cyan QD lies in the band gap alignment of InP/ZnSe(S)/ZnS. The photoluminescence lifetime of our InP/ZnS/ZnS material was a staggering 212 ns. Inclusion of Se can decrease the lifetime at the expense of introducing a ZnSe shell with a type-II band alignment with InP. Alternative materials such as ZnSeTe-based QDs, highly engineered shells, or innovative InP alternatives may enable cyan Cd-free QD emitters.

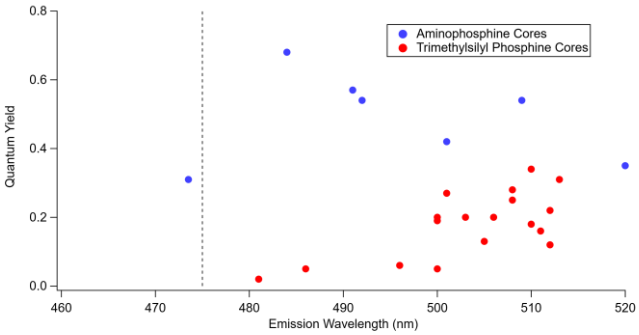

Figure 3. Experiments at OSRAM (blue dots) and Columbia (red dots) varying core/shell structure, zinc precursor, and ZnS reaction temperature. The target of 475 nm emission is depicted by the dashed grey line.

IIIA.3 Cd-free QDs for red emission

Utilizing the methodology for cyan-emitting InP has allowed for an adaptation of a previously synthesized seeded growth methodology to grow high quality InP nanocrystals spanning 500–600 nm from the InP seeds. As growth increases, the quantum dots have increased valley-to-depth ratios, a metric associated with good size dispersity (**Figure 4**).

Early in the project, we attempted to improve absorption at 450 nm for red QDs through inclusion of gallium phosphide

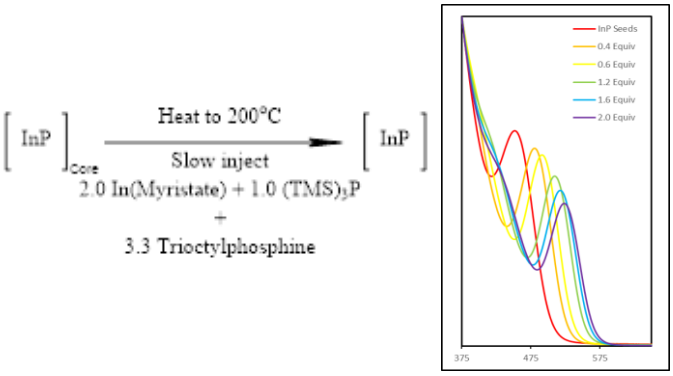

Figure 4. Seeded growth of InP quantum dots from 500 to 600 nm.

(GaP), either during seed synthesis to produce InGaP QDs or through applying a discreet shell of GaP on InP QDs. At OSRAM, both structures were investigated. Drawing on prior work at Columbia and OSRAM from Award Number DE-EE0008716, InGaP synthesis was attempted from indium halides, gallium acetylacetonate, and zinc iodide with the phosphorus precursor tris(diethylamino) phosphine. While this synthetic scheme yielded luminescent In(Ga)P particles, we were unable to confirm the incorporation of gallium using techniques including x-ray diffraction (XRD) and inductively coupled plasma optical emission spectroscopy (ICP-OES).

The InP/GaP/ZnS heterostructure was also investigated, combining *in situ* gallium halides with a slow addition of TMS-P at high temperatures (**Scheme 1**). TEM images and absorption spectra looked promising, indicating deposition of up to 4 monolayers of GaP and an improvement in the OD_{450} of 2× compared to InP alone (**Figure 5**). However, the core/shells did not emit when shelled with a variety of ZnS routes. XRD analysis did not support the synthesis of crystalline GaP; the particle emission likely suffered from numerous surface defects and poor ZnS deposition.

Scheme 1. GaP and ZnS shelling conditions on red InP seeds. 1.1 mmol of GaI_3 was added to 1.9×10^{-3} mmol InP QDs; molar equivalents of ZnI_2 and TMS-phosphine are relative to GaI_3.

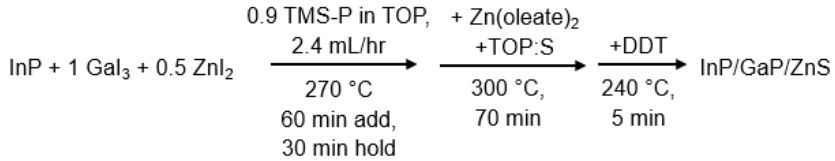

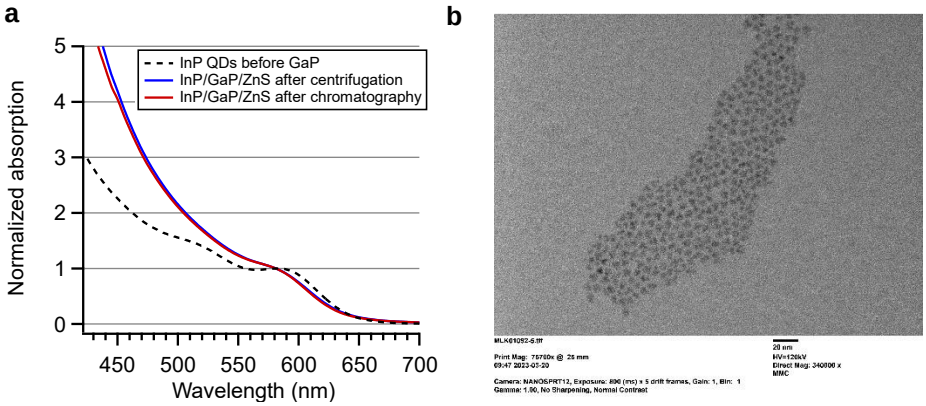

Figure 5. a) UV-Visible absorption spectra for InP and InP/GaP/ZnS QDs. The absorption at 450 nm doubles for InP/GaP/ZnS compared with InP QDs. b) TEM image demonstrates conformal growth of 4 monolayers of GaP material.

Direct heterogeneous synthesis of GaP is a difficult problem, however, work at Columbia during this project demonstrated that crystalline GaP is possible through an alternative route. Crystalline GaP can be readily accessed by reacting phosphorus precursors with liquid metal gallium nanodroplets to form various morphologies: wires, teardrops, and spheres. The high level of crystallinity afforded by this method is unmatched compared to more traditional molecular syntheses, such as the dehalosylation route. However, these reactions are heterogeneous where GaP formation is templated by the Ga nanoparticle. This limits size, morphology, and composition control. We aimed to obtain a better understanding of the reactivity of the Ga nanoparticle intermediate, how the crystallization pathway can be influenced, and how to access alloy and heterostructure products such as InGaP or InP/GaP toward Subtasks 1.2 and 1.3.

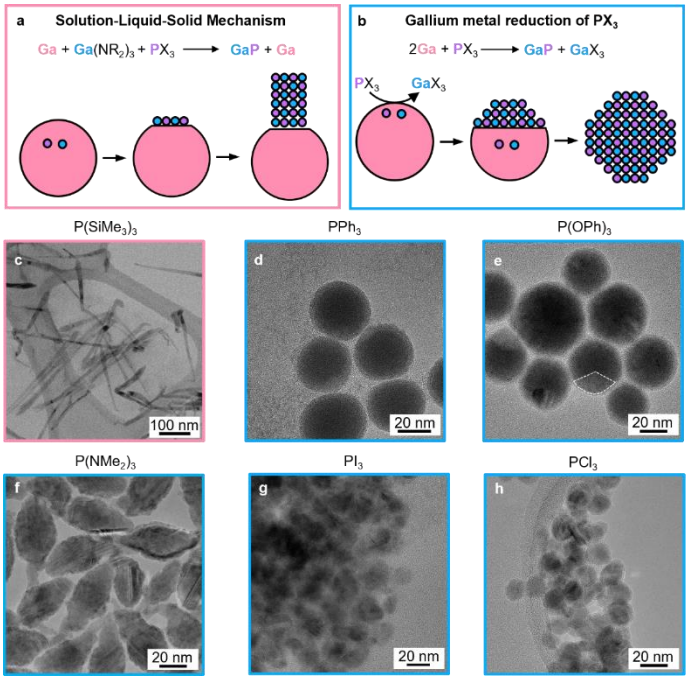

Figure 6. Illustration of (a) the catalytic wire growth enabled by the SLS mechanism and (b) GaP formation via gallium metal reduction of PX_3. TEM images of GaP synthesized with PX_3 = (c) $P(SiMe_3)_3$, (d) PPh_3, (e) $P(OPh)_3$, (f) $P(NMe_2)_3$, (g) PI_3, and (h) PCl_3.

We have identified two possible reaction pathways through Ga metal to form GaP. One is the solution-liquid-solid (SLS) mechanism where GaP nanowires are produced via catalytic growth from a metal nanoparticle (**Figure 6a**). Here, Ga^{3+} and P^{3-} species first dissolve into a liquid nanodroplet. Then, once supersaturation is reached, nucleation and growth occur at the liquid-solid interface. This method results in wire growth as the metal nanodroplet acts as a catalyst and is not depleted during the reaction.

Alternatively, GaP can be crystallized via gallium metal reduction of PX_3, where the phosphorus precursor is introduced in a P^{3+} state (**Figure 6b**). Here, the necessary Ga^{3+} and P^{3-} precursors are generated via a redox reaction at the surface of the Ga metal. Upon oxidation of Ga and reduction of PX_3, crystallization of GaP occurs in a process similar to the SLS mechanism but limited by the supply of Ga metal. This method of GaP crystallization allows access to various nanocrystal morphologies and controls the reaction mechanism by changing the driving force via the formation of the GaX_3 coproduct.

To interrogate how these two reaction pathways influence GaP crystallization, we reacted Ga metal with different PX_3 precursors. The PX_3 precursors evaluated herein were tris(trimethylsilyl) phosphine ($P(SiMe_3)_3$), triphenylphosphine (PPh_3), triphenylphosphite ($P(OPh)_3$), tris(dimethylamino) phosphine ($P(NMe_2)_3$), phosphorus triiodide (PI_3), and phosphorus trichloride (PCl_3). After reaction with $P(SiMe_3)_3$, long nanowires of GaP are formed (**Figure 6c**), suggesting an SLS-mechanism of GaP growth. Full conversion of the gallium precursor likely has not occurred upon phosphorus injection, leaving accessible Ga^{3+} in the solution. These Ga^{3+} species readily combine with P^{3-}, introduced from the $P(SiMe_3)_3$, within the liquid nanodroplet and undergo catalytic wire growth.

Reaction with the other phosphorus precursors (PPh_3, $P(OPh)_3$, $P(NMe_2)_3$, PI_3, and PCl_3) result in a departure from the nanowire geometry. PPh_3 has the slowest reactivity with gallium metal; after heating at 280 °C for 48 hours, little to no conversion to GaP is observed (**Figure 6d**). $P(OPh)_3$ showed increased reactivity, but only a small fraction of the Ga metal was converted to GaP (highlighted with a white dashed line) after 48 hours (**Figure 6e**). A marked jump in reactivity occurs with $P(NMe_2)_3$—all the Ga metal converts after just 1 hour of reaction and forms GaP with teardrop shapes (**Figure 6f**). PI_3 and PCl_3 show a further increase in reactivity as the Ga metal is fully converted 10 minutes after injection (**Figure 6g** and **6h**). Additionally, these nanocrystals are the smallest in size and have a spherical morphology. The departure from the SLS mechanism is unsurprising as these precursors introduce phosphorus in a 3+ oxidation state, thus necessitating the Ga metal reduction of the PX_3 to generate GaP. The reactivity of PX_3 with Ga metal should be dictated by a combination of three components: stability of the phosphorus precursor, Lewis

acidity of the phosphorus precursor, and stability of the GaX_3 coproduct. The rapid reactivity with PCl_3 is likely driven by its relatively weak P-Cl bonds, high Lewis acidity, and stability of the produced $GaCl_3$.

To further explore the reactivity of PCl_3, the reagent ratios were varied between P/Ga = 1/3, 1/2, 1, and 3. TEM images of the nanocrystals are shown in **Figure 7a-d**. Interestingly, at low equivalents of P (P/Ga =1/3 and 1/2), wire and teardrop nanocrystals are formed. At P/Ga = 1, hollow nanocrystals are produced, likely a consequence of the nanoscale Kirkendall effect. At P/Ga = 3, small spherical GaP is observed, similar to the P/Ga = 2 reaction, however, they are now embedded in an amorphous matrix. These results imply that the crystallization mechanism of GaP is controlled by the concentration of PCl_3. Importantly, there is a distinct change in nanocrystal size and morphology at P/Ga = 2 which may indicate a departure from a heterogeneous reaction mechanism. We hypothesize that high concentrations of PCl_3 may drive dissolution or nanocrystal etching.

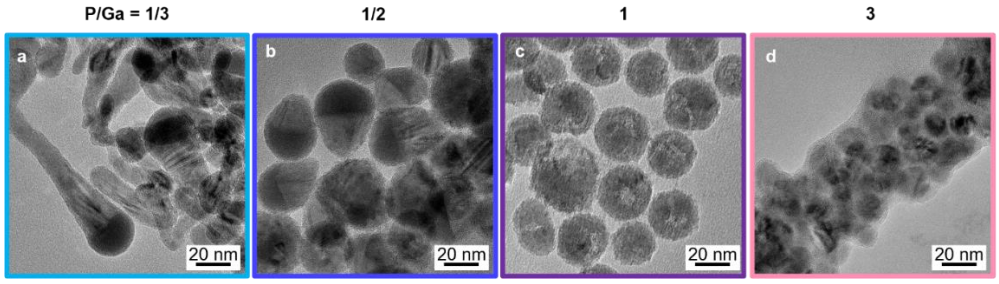

Figure 7. TEM images of GaP grown via injection of PCl_3 into a solution of Ga nanoparticles that were grown at 280 °C for 2 minutes. P/Ga = (a) 1/3, (b) 1/2, (c) 1, and (d) 3.

Surprisingly, the reaction of PCl_3 with large 35 nm Ga nanoparticles resulted in small, spherical GaP nanocrystals of size 15 ± 2 nm (**Figure 8**). Additionally, phosphidation was rapid and complete 30 seconds after injection of the PCl_3. High-resolution TEM images indicate that the Ga particles are completely converted to GaP as lattice fringes are observed over the entire area of the GaP nanocrystal (**Figure 8c**). XRD analysis confirmed the presence of crystalline GaP. On the timescale of this project, this novel GaP chemistry was not interfaced successfully with the In-based core/shell heterostructures. However, this sub-project is immensely valuable to those attempting to understand the formation of crystalline GaP and the potential of the material for improving blue absorption of Cd-free QD materials.

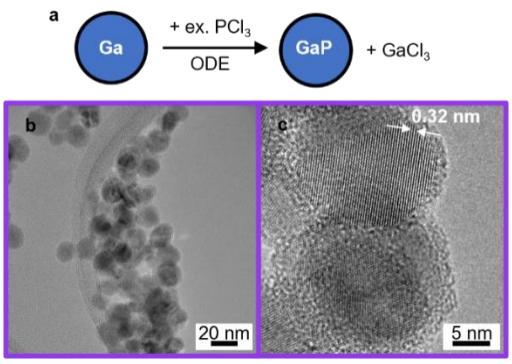

Figure 8. (a) Formation of GaP upon the reaction of Ga with PCl_3. (b) TEM image of resulting GaP nanocrystals formed 30 seconds after PCl_3 injection. (c) High-resolution TEM image of GaP nanocrystals showing lattice fringes corresponding to GaP (111) planes.

Despite challenges obtaining InGaP and InP/GaP particles, bright red-emitting InP/ZnSe/ZnS QDs were realized within this project. Toward the aim of making LEDs with improved performance reliability, we have developed control of ZnSe(S) and ZnS deposition on InP QDs. The primary approach we used was comprised of a high temperature precursor addition scheme, with variable addition rates to control the composition of the Se/S gradient. We experimented with variables such as precursor identity, chalcogenide mixture, addition rate, reaction hold time, shell thickness, and addition temperature.

In one study, we deposited various thicknesses of ZnSe shells. Purified InP/ZnSe QDs display a clear increase in the absorption at 450 nm with ZnSe shell thickness (**Figure 9**). Absorption at 450 nm is important for QD-LED down-conversion; ZnSe deposition on red QDs is one established strategy to increase absorption. Notably, each sample red-shifts by the same amount, indicating that the red-shift is due to a surface effect resulting from templating of the ZnSe material on the InP QD, and is not influenced by ZnSe growth past the first monolayer.

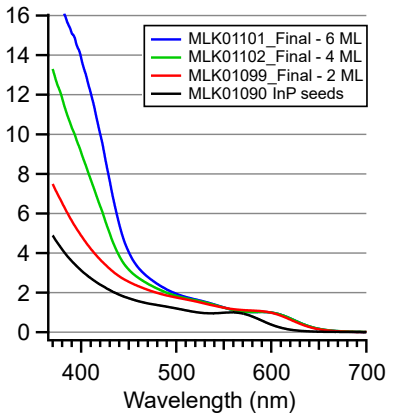

Figure 9. Normalized absorption spectra for InP QDs shelled with 2, 4, and 6 monolayers of ZnSe.

Next, developments aimed at enabling a smooth ZnSe-to-ZnS transition gradient at the monolayer level. A smooth gradient between intermediate and exterior shells (here ZnSe to ZnS) has been identified by multiple research groups as an ideal structure to reduce strain, decrease likelihood of trap formation, and suppress Auger recombination (**Figure 10**). The smoothest ZnSe-to-ZnS gradient on InP we have seen in the literature appears to be a three-step gradient over possibly 10 monolayers. We primarily utilized $ZnCl_2$, S:TOP, and Se:TOP as ZnSeS precursors, targeting different intermediate shell architectures (ZnSe, ZnSeS alloys, and ZnSeS gradients). Through syringe pump addition, we found that synthesizing the intermediate shell at 330 °C and the exterior ZnS synthesis at 300 °C led to the best performing QDs. By the end of this project, we obtained red-emitting QDs with ~70–80% PLQY at 620–630 nm and with FWHM values of <50 nm.

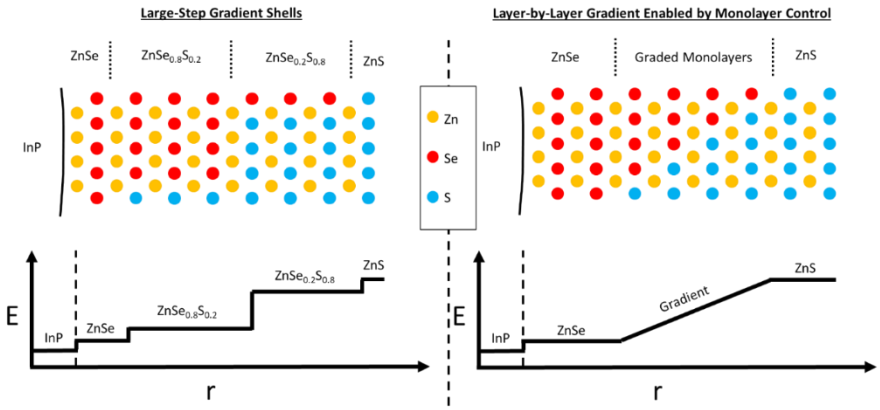

Figure 10. (left) Literature shelling methods use large-step gradient ZnSeS shells. (right) Targeted grading of the $ZnSe_ySx$ shell by tuning each monolayer.

IIIB. Improve QD Stability via Surface Passivation

IIIB.1 Facet Control during Core/Shell Synthesis

The stability of InP/ZnSe/ZnS QDs on-chip is crucial, as the QDs are faced with high flux, high temperature, ambient atmosphere, and matrix challenges. We proposed that the {100} facets of zinc blende crystal lattices would be strongly ligated and thermodynamically stable, which would afford higher chemical and flux stability to the ZnS surface compared with {111} facets. InP/ZnSe/ZnS QDs terminated by {100} facets have a cube-shaped morphology, whereas {111} facets yield a tetrahedral morphology (**Figure 11**). Spherical

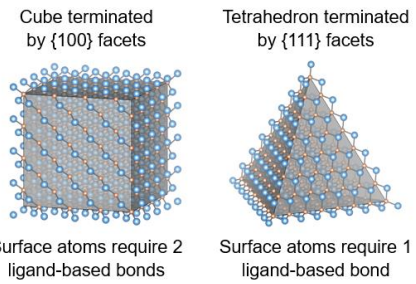

Figure 11. Coordination environments of {100} and {111} surface facets.

morphologies are a combination of {100}, {111}, and {110} facets. Selective control of a particular facet is desirable as it can inform how certain reagents influence the growth of ZnSe and ZnS shells.

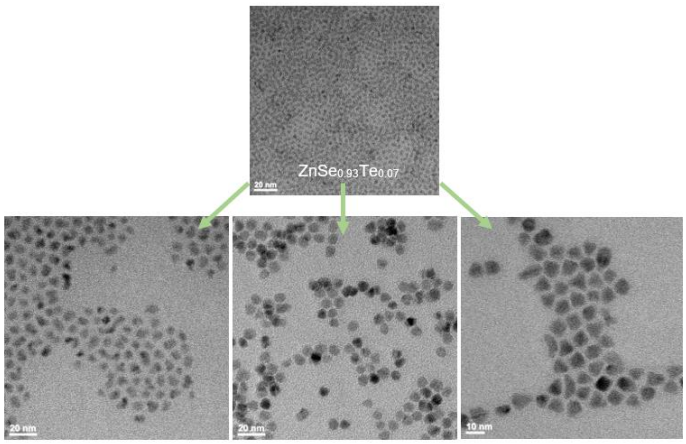

Figure 12. Various ZnSe/ZnS shelling protocols on ZnSeTe QDs.

Halides and carboxylates have been shown to drive the formation of {100} facets in Cd-based and ZnSeTe systems. As a model system, we first achieved {100} facet growth in a fully II-VI system, ZnSeTe/ZnSe/ZnS, by employing multiple ligand systems, including chloride/oleate and oleate/oleic acid (**Figure 12**). Both systems employed $Zn(oleate)_2$ synthesized from $Zn(acetate)_2$ without isolation of the pure salt; acetate may have been a crucial ligand in these systems.

Next, we transferred the ZnSe and ZnS shelling principles from the ZnSeTe QD system to make InP/ZnSe/ZnS cubes. Increasing concentrations of $ZnCl_2$ yielded more cube-shaped morphologies, as predicted (**Figure 13**). However, the optical properties of oleate-capped QDs suffered during the shelling conditions employed, so $Zn(acetate)_2$ was also investigated. In the sample using 10x $Zn(acetate)_2$, cubes were not evident, with most particles adopting a tetrahedral or quasi-tetrapodal morphology (**Figure 13**). However, these particles were the brightest obtained within this facet control project, at 83% PLQY, 609 nm centroid, and 52 nm FWHM (**Table 1**).

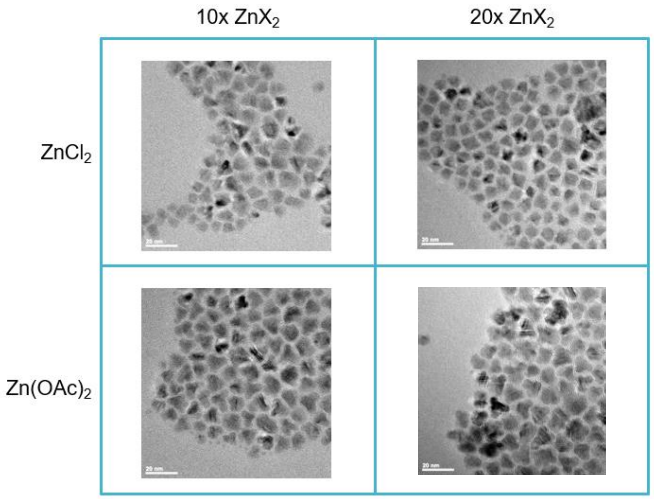

Figure 13. TEM images for QDs shelled with various amounts of zinc salts present.

Table 1. Optical properties for InP QDs shelled in the presence of $ZnCl_2$ or $Zn(OAc)_2$

Structure	Sample	PLQY (%)	Centroid (nm)	FWHM (nm)	Lifetime (ns)	Radiative Rate	Non-Radiative Rate
InP/ZnSe/ZnS	1x $ZnCl_2$	69	599.9	46.3	36.5	15.6	11.8
InP/ZnSe/ZnS	10x $ZnCl_2$	24	605.0	57.1	47.1	4.3	16.9
InP/ZnSe/ZnS	20x $ZnCl_2$	14	611.4	51.7	-	-	-
InP/ZnS	10x $Zn(OAc)_2$	50	593.7	63.8	67.7	7.2	7.6
InP/ZnSe/ZnS	10x $Zn(OAc)_2$	83	608.6	52.1	39.7	19.5	5.7
InP/ZnSe/ZnS	20x $Zn(OAc)_2$	69	609.1	51.3	41.5	15.5	8.6

IIIB.2 Post-Synthetic Ligand Exchange

Recently, we have published work from a sub-project within this grant on the topic of surface fluorination reactions with InP QDs.[a] Proper passivation and elimination of surface defect sites such as undercoordinated indium yield improved PLQY values and provide a suitable platform for the encapsulation of InP QDs with zinc chalcogenide shells for long-term on-chip stability. However, the effect of surface ligands and other surface chemistry-based etching or passivation techniques is underexplored and often done without a molecular-level understanding. Photochemical etching of an InP QD in the presence of benzoyl fluoride can drastically improve PLQY and FWHM by undergoing size selective etching. This surface treatment can be seen as an anhydrous analogue to the common hydrofluoric acid etching procedure and occurs via the *in situ* generation of oleylammonium fluoride (**Scheme 2**).

Scheme 2. Generation of oleylammonium fluoride from benzoyl fluoride and oleylamine

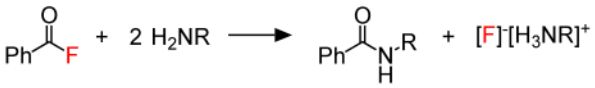

Photochemical etching is a post-synthetic tool to decrease size and prepare a nanocrystal surface for efficient epitaxial shell growth by promoting the formation of an even initial monolayer of zinc chalcogenide on the InP surface. This monolayer, however, is directly inhibited by the formation of surface indium oxide which rapidly forms in conditions such as washing in open air with wet solvents like ethanol or acetone. This change has been commonly ignored in the current literature despite the rapid oxidation of InP evidenced by the generation of phosphate groups on InP surfaces. In response, we synthesized oxygen-free InP using aminophosphine and metal halides and took care not to expose the QDs to air. Careful analysis of the InP purification procedure via ^{1}H and ^{31}P NMR spectroscopy indicated that in solution, the ligand structure is complex. Instead of the X-type/L-type ligand surface environment of chloride and oleylamine ligands, the ligands are better characterized as an X-type ion pair on the surface of the QD, described as a tetra(oleylamino)phosphonium chloride ($P[NHR]_4Cl$) surface ion pair (**Figure 14**).

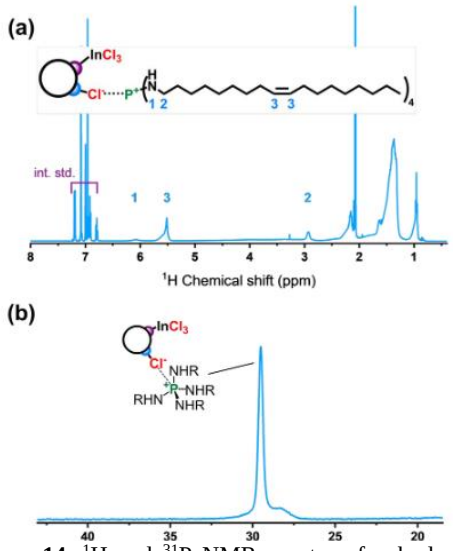

Figure 14. ^{1}H and ^{31}P NMR spectra of anhydrous washed InP QDs showing an InP QD with a tetra(oleylamino)phosphonium chloride surface ligands.

The bound ion pair $P[NHR]_4Cl$ can be displaced by oleylammonium fluoride. In addition, fluorination of surface indium ions was shown to occur. Reaction of the fluorinated surface with trimethylsilyl chloride liberated fluoride ions, crucially demonstrating that fluoride was bound to the QD surface (**Figure 15**). X-ray photoelectron spectroscopy (XPS) supported the formation of InF_3 coproducts during this reaction. We hypothesize that metal fluoride adsorption to the QD surface enhances the PLQY by changing the band edge potential. Importantly, this mechanism contrasts with removal of surface oxides in the presence of HF or other fluoride sources, suggesting that passivation of surface indium ions is a more effective strategy to boost PLQY.

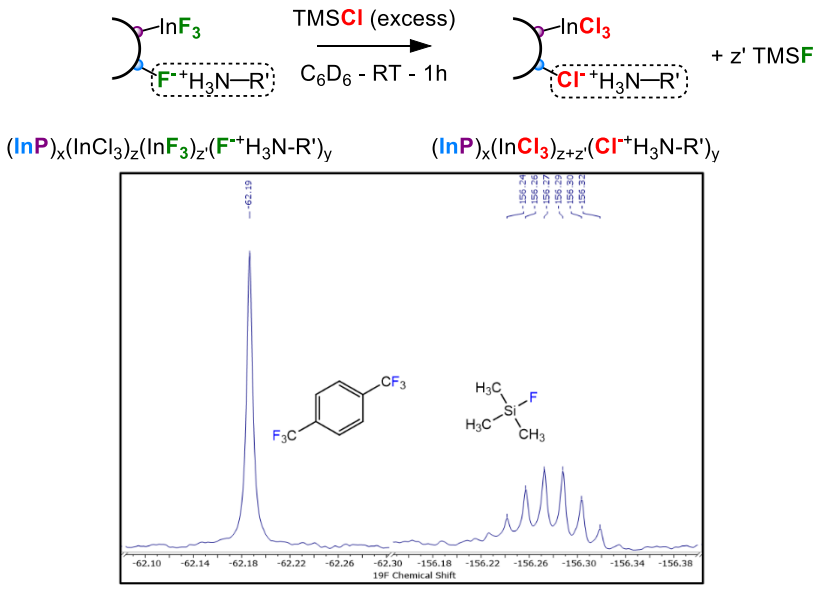

Figure 15. Reaction scheme of the surface exchange of etched InP QDs utilizing TMS-Cl and corresponding peaks of bis(trifluoromethyl) benzene internal standard and the ^{19}F signal of TMS-F.

Fluorination of core/shell materials was also investigated using aminophosphine-derived InP cores with a ZnS shell. The PLQY of the core/shell was enhanced by 2.5x upon fluorination of the ZnS surface. The ZnS shelling was carried out using $Zn(oleate)_2$ as the Zn precursor; Zn carboxylates can readily react with fluoride. Due to the potential unwanted reaction between $Zn(oleate)_2$ and oleylammonium fluoride, the fluorination reaction condition required additional optimization to determine the optimal concentrations of $Zn(oleate)_2$ and oleylammonium fluoride. Collaboration between Columbia and the Molecular Foundry has identified both concentration dependence and kinetic effects of the reaction between InP/ZnS and fluorination precursors (**Figure 16**).

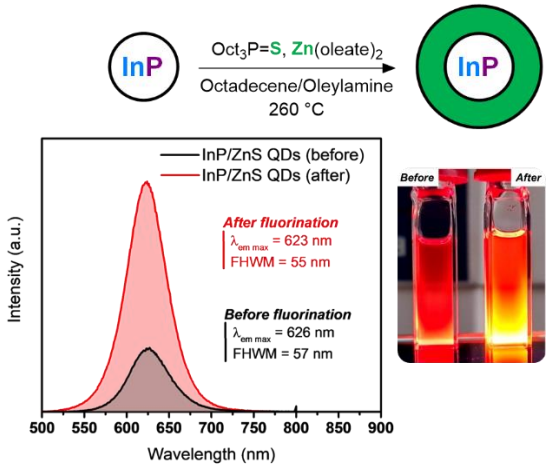

Figure 16. Schematic summarizing the ZnS shelling reaction to obtain the InP/ZnS core/shell nanocrystals. PL spectrum evolution highlighting the 2.5x enhancement of the PL intensity of the QDs. Images of the QD suspension under UV light excitation (l_{exc} = 365 nm) before and after the surface treatment.

High-throughput (HT) fluoride treatment screening at the Molecular Foundry with the robot HERMAN provided a helpful foundation for future campaigns. The performed workflow demonstrated the generalizability of our HT experimental workflow developed throughout the project as an efficient screening tool to measure optical merits of QDs as they are exposed to various compounds at a range of concentrations and times. The PL intensity of InP/ZnS QDs as a function of oleylammonium fluoride and zinc oleate concentrations showed interesting multiple combinations of the two reagents that can lead to high PL intensity. We found that while PL peak position and FWHM are relatively stable during 14 hours of fluoride treatment at room temperature, PL intensity decreased 51%, suggesting extended exposure to fluoride treatment can be detrimental to the PL intensity of QDs.

In addition to the overall increase in the PL intensity, mapped reagent concentrations revealed PL maxima that were dependent on light irradiation (**Figure 17**). HT fluoride treatment under accelerated conditions (427 nm, 3 hours) showed an average 37% increase in relative PL intensity throughout the reagent concentrations surveyed. The global maximum of PL intensity was initially found in the low concentration region of zinc oleate. After light irradiation, this maximum moved to higher zinc oleate concentration regions. This delayed increase in the PL intensity at high concentration of zinc oleate suggests that the conversion or adsorption of zinc oleate can be a rate limiting step of the fluoride treatment reactions that increase the PL of InP/ZnS QDs. To better understand the role of these reagents, additional screening of the conditions of fluoride treatment is underway.

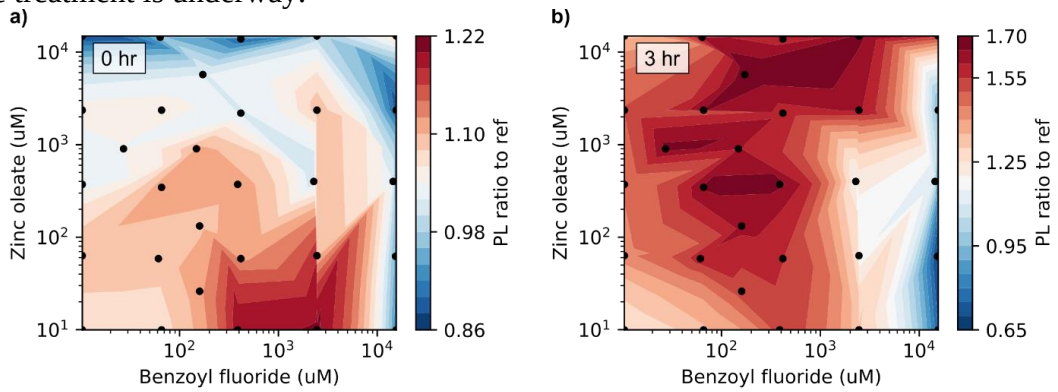

Figure 17. The contour plot of the relative PL peak intensity of InP/ZnS QDs as a function of benzoyl fluoride and zinc oleate concentration. Oleylamine to benzoyl fluoride was fixed at the ratio 2:1. PL spectra were collected after InP/ZnS QDs were exposed to etching reagents for a) 0 hours and b) 3 hours. PL spectra were collected with an excitation wavelength of 410 nm. For the 3-hour etching, prepared reactions were placed in a light box with blue light (427 nm) for 3 hours.

IIIB.3 QD Surface Performance Studies

To enable the use of Cd-free quantum dots in LEDs for human-centric lighting, we needed to understand how best to generate QDs that would survive both the process of making the LEDs and, subsequently, the operation of the LEDs. Because we were starting the project with QDs that could survive neither process, we developed a chemical challenge and a blue-light flux challenge to further interrogate the ability of the QDs to retain their PLQY as specified in Milestone 2.3.1. These challenges enabled us to screen various types of QDs, including (but not limited to) commercial Cd-based QDs from OSRAM, InP or InZnP cores, gallium-containing processes, and core/shells with various thicknesses of ZnSe and ZnS.

For the chemical challenge, we developed a library of LED-relevant chemicals to investigate different hypothetical QD degradation pathways via chemical and/or quenching mechanisms. For the test, different QD batches were diluted to the same concentration and were then exposed to specified concentration of the challenge chemicals and stirred in air over 24 hours. The chemicals and concentrations chosen for the final panel screening enabled us to observe a dynamic range of responses over several hours to days. Different QD architectures showed varying responses to different challenge chemicals. Examples of PLQY retention over 24 hours in three batches of QDs are given in **Figure 18**.

Due to the known challenges of Cd-free QD stability under flux in air and during LED curing in air, we additionally developed a method of exposing QDs in solution to 450 nm light at a constant flux. We chose a flux that gives a dynamic range of PLQY degradation so we can better understand how changes to the QD architecture affects flux dependence, as demonstrated in **Figure 19**. As in the chemical challenge, different architectures degrade at various rates upon exposure to 450 nm flux. One example from the facet control work described above shows that InP/ZnS is much more stable than Se-containing particles (**Figure 19**). Often, whether a sample contains Se determines its performance on the flux test, though some of this effect can be negated through application of very thick ZnS shells.

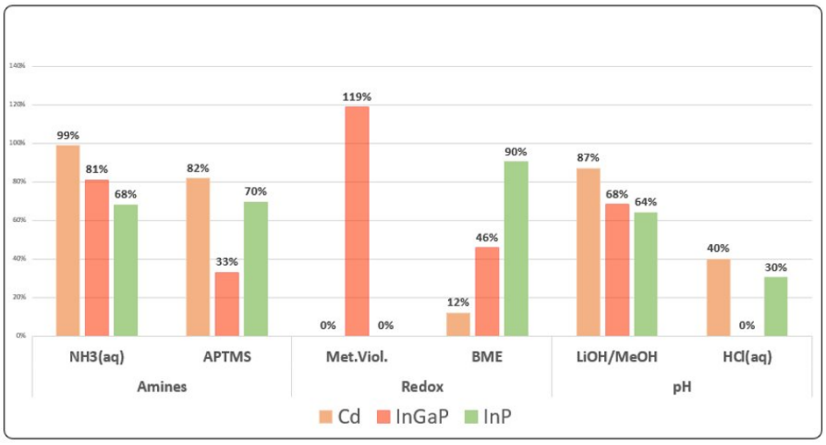

Figure 18. PLQY retention after 24 hours of exposure to challenge chemicals for three different QD architectures.

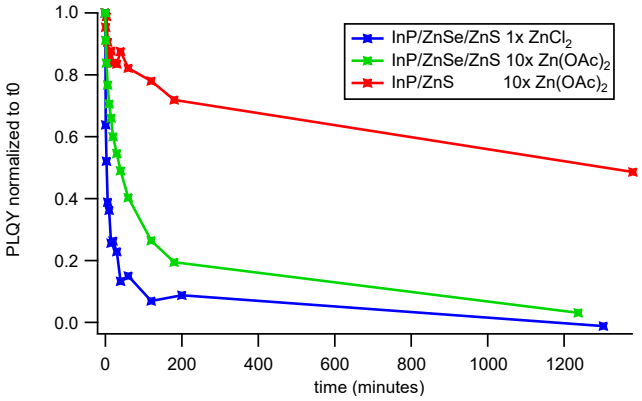

Figure 19. 24-hour PLQY retention under low blue flux.

To further probe the impact of the ZnS shell on chemical and flux stability, we synthesized Se-containing and Se-excluding QDs. As demonstrated in **Table 2**, thicker exterior ZnS improves PLQY retention under both flux and hydrochloric acid stress tests. Very thick ZnS on the top of thin $ZnSe_xS_{1-x}$ can recover some light and chemical performance lost due to the presence of Se in the intermediate shell. Furthermore, thick ZnS-coated InP has enabled barrier chemistry research due to the chemical stability of the QDs, as described in the next section.

Table 2. Effects of intermediate $ZnSe_xS_{1-x}$ shell and ZnS shell thicknesses on solution flux test and HCl quench test

Intermediate $ZnSe_xS_{1-x}$ Monolayers	ZnS Monolayers	PLQY	Flux test, 24hr retention	HCl Retention
0	<1	0.54	6%	0%
0	2	0.54	22%	20%
0	15	0.52	53%	58%
1.7 gradient ZnSeS	1.4	0.56	10%	0%
~2 $ZnSe_{0.5}S_{0.5}$	7.7	0.69	14%	3%
~2 $ZnSe_{0.5}S_{0.5}$	13.5	0.65	37%	20%

IIIC. Novel Barrier Coatings for QDs
IIIC.1 Calcium and Zinc Phosphate

Metal-oxide encapsulation is one method to stabilize QDs in on-chip applications. However, OSRAM's proprietary ultrabarrier technology quenches III-V QDs when transferred directly from Cd-based systems, indicating a buffer layer may be needed between the QD and the metal oxide encapsulant layer. The buffer layer needs to be mechanically robust, chemically stable, and compatible with the quantum dot and existing metal oxide encapsulation techniques. To this end, we explored metal phosphates as barrier coatings. Controlled growth of an amorphous calcium phosphate (ACP) layer on the surface of QDs could lead to better protection of QDs against harsh conditions that are required for commercial QDs to survive. For example, the formation of ACP only near the surface of QDs could lead toward shell-like growth of ACP on QDs, providing an additional layer of protection while maintaining colloidal stability. If the PO_4 source was limited to the surface, added Ca would form $CaPO_4$ only at the surface of QDs.

Preparing phosphate-capped QDs is the first step towards metal-phosphate-encapsulated QDs. This was done using phosphoric acid in *N*-methylformamide as the phosphate source. A mixed solvent system was used, where *N*-methylformamide was used to solubilize the phosphate-capped quantum dots and cyclohexane was the carrier solvent for the QDs before ligand exchange. Successful ligand exchange was accompanied by a change in solubility with little change in the absorption spectrum (**Figure 20**). Good colloidal stability of QDs suspended in *N*-methylformamide (NMF) suggests a successful ligand exchange from the initial non-polar long carbon chain ligand to phosphate ions.

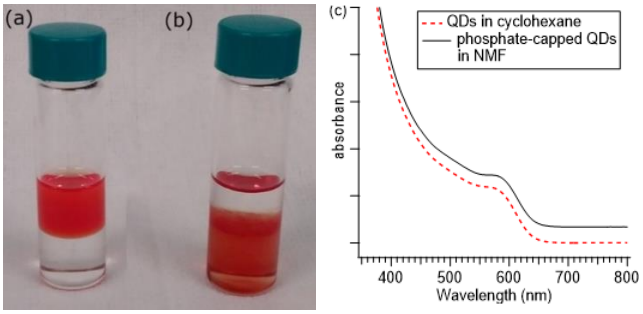

Figure 20. a) QDs in cyclohexane above *N*-methylformamide prior to ligand exchange. b) QDs in *N*-methylformamide below cyclohexane after ligand exchange. c) Representative UV-Vis spectra of as-synthesized and phosphate-capped QDs (offset).

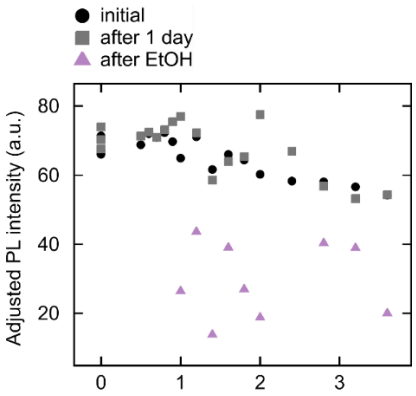

Figure 21. InP/ZnS QD solutions with PO_4 capping ligand incubated in various concentrations of $CaCl_2$ solution in NMF. The absorption and PL spectra were measured right after Ca addition (black), after 1 day of incubation (gray), and after ethanol-induced precipitation followed by redissolution in NMF (purple).

In collaboration between OSRAM and the Molecular Foundry, we assessed the effects of Ca addition on phosphate-capped QDs. As shown in **Figure 21**, various concentrations of $CaCl_2$ solution ranging from 0.5 to 3.6 Ca:P ratio showed a decrease in adjusted PL intensity to 80% of initial PL, suggesting excessive amount of $CaCl_2$ should be avoided to maintain PL intensity of QD during ACP treatment. We also tested ACP precipitation with EtOH to form precipitates that successfully captured QDs. The size of the QD embedding matrix was small enough to be re-dissolved back into the solution, providing a relative QY retention of ca. 42%.

To characterize the structure of amorphous calcium phosphate (ACP) and amorphous zinc phosphate (AZP) buffer layers on InP/ZnS QDs, samples were prepared at OSRAM and sent to Molecular Foundry for imaging and X-ray diffraction

analysis. After drying in vacuum, ACP and AZP composites were obtained in bulk solids. The SEM images of three samples, bulk ACP (blank), InP/ZnS QD@ACP composite, and InP/ZnS QD@AZP composite are shown in **Figure 22**. The observed similarities between ACP samples may suggest that the embedding QD did not affect the macroscale structure during the formation of ACPs. In contrast, observed flat surfaces of InP/ZnS QD@AZP composite in macroscale suggests that propagations of AZP composite fracturing were much longer and more ordered compared to ACP composites.

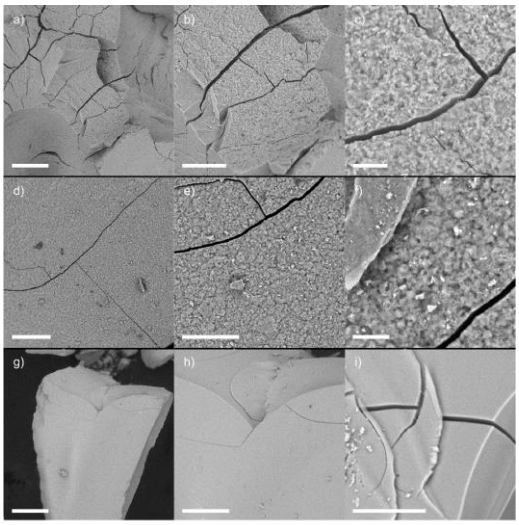

Figure 22. SEM images of amorphous metal phosphates. a-c) InP/ZnS QD@ACP composite, d-f) bulk ACP, and g-i) InP/ZnS QD@AZP composite at different magnifications. Scale bars are 200 µm, 100 µm, and 20 µm from left to right.

In sum, we were unable to controllably deposit metal phosphate buffer layers on a per-particle basis. Because of the massive amounts of amorphous metal phosphate present in these materials and difficulty in isolating the QDs from excess barrier material, we would be unable to load high enough concentrations of the embedded QDs into LED devices. While we did not attempt to place these materials on-chip, we did test them on film, described in section IIIC.3.

IIIC.2 Metal Oxides and Porous Glass

Besides metal phosphate barriers, we investigated infusion of QDs into porous glass to protect QDs from oxygen- and flux-induced degradation mechanisms. Toward successful porous glass infusion with QDs, we aimed to demonstrate the following: 1) confirmation of infusion, 2) PLQY retention after infusion, and 3) enhanced stability under flux.

Permeation method and QD ligand polarity both affected QD incorporation into the porous glass. First, confocal microscopy investigations suggested that QDs in nonpolar solvents were never successfully placed in the pores. Secondly, even with polar solvents we only collected encouraging data with 6-mercaptohexanol (6-MHA) capped QDs in octanol, and then only using the “incipient wetness method” and “vacuum infusion method”. These methods relied on addition of concentrated QD solution to the glass, followed by exposure to vacuum in the case of vacuum infusion. The solvents DMSO and DMF as well as the “prolonged infusion method”, wherein porous glass was saturated first with solvent followed by QD solution, did not give data consistent with incorporation of QDs into the porous glass. **Figure 23** shows the difference between unsuccessful and successful incorporation of QDs into porous glass.

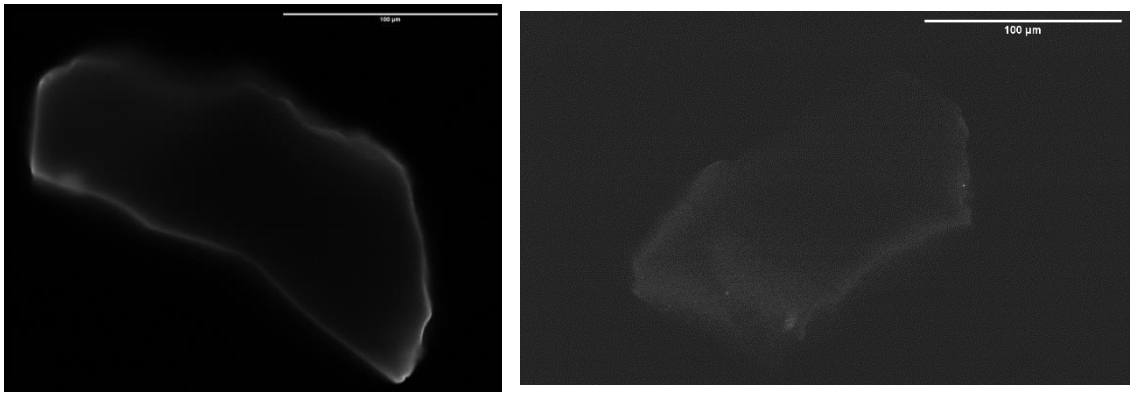

Figure 23. Confocal microscopy images showing a cross section (comprising the edge and interior) of porous glass materials. The left image shows fluorescence originating only at the edges of the porous glass shard. The right image shows fluorescence at the edges but also at the interior of a porous glass shard, consistent with successful infilling of QDs into the pores of the glass.

Porous glass/QD composites exhibited high PLQY retention, over 90%. We found that the major factor in high PLQY retention was thickness of the ZnS shell, as shown in **Table 3**. InP/ZnSeS only retained 7% PLQY after infusion, whereas 15 monolayers of ZnS (shell thickness of ~5 nm) retained 83–92% PLQY.

Table 3. PLQY of QD materials with various amounts of ZnS shell before and after infusion into porous glass

ZnS thickness	Starting solution PLQY	Powder PLQY after porous glass treatment (%retention)
0 (ZnSeS shell)	43%	3% (7%)
<1 monolayer	61%	13% (21%)
~2 monolayers	53%	21% (40%)
~15 monolayers	52%	43% (83%)
Repeat of ~15 monolayers	52%	48% (92%)

Next, we endeavored to seal the pores and carry out reliability testing under blue flux to determine whether the QDs in porous glass performed better than QDs without any additional protection, than QDs in porous glass with pore-sealing chemistry, or than QDs treated with only pore-sealing chemistry (**Figure 24**). Quantum dot materials were illuminated with 450 nm light at an intensity of 60 mW cm^{-2} under ambient atmospheric conditions over 24 hours.

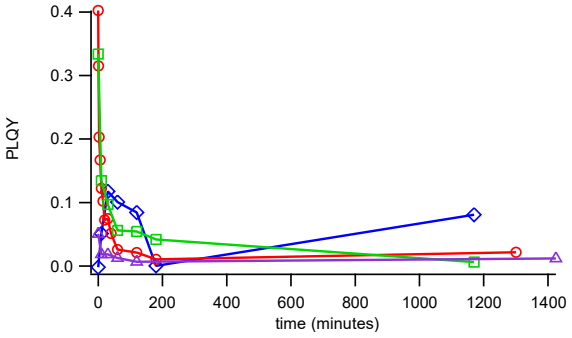

Figure 24. QDs without any additional protection (red circles); QDs inside porous glass (green squares); QDs inside porous glass with pore-sealing chemistry (blue diamonds); and QDs treated only with pore-sealing chemistry (purple triangles).

For all samples *except* quantum dots inside porous glass with pore-sealing chemistry, the PLQY retention as a function of time under illumination exhibited qualitatively the same behavior. The PLQY started at its highest point at t=0 and decayed monotonically. The t=0 PLQY was reasonably high for quantum dots in solution, and QDs inside porous glass, but started at a low level (PLQY ~0.05) for quantum dots treated only with the pore-sealing chemistry. QDs inside porous glass with pore-sealing chemistry exhibited different behavior. Here, the QDs

appeared fully quenched at t=0 after which a modest amount of brightening (PLQY increase) under 450 nm illumination took place during the first 30 minutes. Then, until 3 hours of illumination, the PLQY decreased again. At approximately 20 hours, the sample showed a measureable PLQY again. Additionally, the amount of light absorbed stayed essentially constant for all samples at all time points, indicating that the samples were not chemically degrading.

This is a limited dataset but a few correlations that could form the basis of testable hypotheses can be observed from the available data, as follows: 1) Porous glass incorporation did not significantly deteriorate the quantum dots and may even offer a minor degree of protection against degradation under blue-light illumination. 2) Porous glass incorporation affected how the quantum dots fared after being subjected to pore-sealing chemistry. 3) Porous glass incorporation and pore sealing chemistry resulted in a complex behavior attributable neither to the pore-sealing chemistry or glass infusion alone; the brightening is an emergent effect. The results are scientifically interesting but ultimately, they do not provide an attractive path to protect the quantum dots from environmental attack. After reviewing the data, we have decided not to pursue this branch of research.

IIIC.3 Barrier-Coated QD Performance in Film

To make HCL LED devices, QDs must survive the silicone curing process. From observations throughout this project, ligands on the surface of the ZnS shell greatly impact whether the silicone cures. In conjunction with a barrier layer, calcium phosphate, we tested the effect of ZnS surface ligands on both the efficacy of calcium phosphate deposition and on silicone curing. We synthesized one batch of red In(Zn)P then deposited approximately 14 monolayers of ZnS, the surface of which is primarily ligated by oleylamine (OLAM) and zinc chloride. Before purification, this batch of QDs was split into thirds: one third was extracted and purified, one third received an injection of 1-dodecanethiol (DDT), and one third received an injection of zinc oleate dissolved in oleylamine and octadecene.

We presume that all three QDs have some amount of oleylamine (L-type) and $ZnCl_2$ (Z-type) ligands, with the two further-functionalized core/shells undergoing some extent of ligand exchange with additional capping by either 1-dodecanethiolate (X-type), 1-dodecanethiol (L-type), or zinc oleate (Z-type). Previous work in this project has shown that 1-dodecanethiol(ate) is much harder to remove from the surface than oleylamine, zinc oleate, or zinc chloride. We therefore hypothesized that thiolate ligands may prove difficult for the phosphoric acid to completely remove the thiolate ligands before calcium phosphate deposition. The three QDs had very similar PLQY, centroid, and FWHM values (**Table 4**). This suggests that any differences between the properties of the three QDs post-encapsulation are a direct result of the surface ligand on the phosphate reaction.

Table 4. PLQY measurements at each stage of the calcium phosphate reaction

QD-Native ligand	PLQY QD-Native ligand (%)	PLQY† QD-PO_4 (%)	PLQY† QD-calcium phosphate (%)	PLQY† in cured silicone (%)	Comments
InP/ZnS- $Zn(oleate)_2$	65	55 (85)	26 (40)	27 (42)	Silicone did not completely cure
InP/ZnS-DDT	64	54 (84)	23 (36)	29 (45)	
InP/ZnS- OLAM	63	–	–	–	unsuccessful ligand exchange

†*PLQY (PLQY retention in % compared to QDs with native ligand set)*

After phosphate exchange, the PLQY retention was ~85% compared to the colloidal QDs with native ligands (**Table 4**). Upon reaction with $CaCl_2$, the PLQY retention dropped to ~40% compared with the starting QDs. Oleylamine-capped QDs were not successfully ligand-exchanged for phosphate and rapidly precipitated to become insoluble in both cyclohexane and *N*-methylformamide.

QD-calcium phosphate samples were dispersed in silicone and cast onto E2835 LED chips. The silicone was heated to a final temperature of 120 °C over 10 hours using a programmed temperature ramp. For the samples where the silicone did not cure, the temperature was increased to 150 °C for an extended period of time but this still did not result in curing. For both $Zn(oleate)_2$-capped and DDT-capped samples, the PLQY of the QD-calcium phosphate material was not harmed during the silicone curing process (**Table 4**). In one case, the samples made from InP/ZnS-DDT QDs showed a modest brightening effect.

These results highlight the importance of QD ligand chemistry on phosphate ligand exchange and device preparation. Only QDs capped with DDT ligands were successfully ligand-exchanged and incorporated into a cured silicone polymer. $Zn(oleate)_2$-capped QDs survived the silicone curing process, but hindered the complete curing of the silicone. Ultimately, we achieved an absolute PLQY of 29% for the InP/ZnS-DDT QDs, which fell short of our project goal of 90%. However, the main source of PLQY quenching occurred during application of the barrier chemistry, and not during the silicone curing process. This finding indicates that the QDs are capable of surviving silicone curing in air at elevated temperatures over hours.

IIID. Performance and Stability Studies of HCL QD-LEDs

IIID.1 LED Light Source

Since the typical pump wavelength of 450 nm used in commercial devices is very close to the emission peak of cyan QDs, it was necessary to study whether it would be beneficial to the color metrics to switch from 450 nm for the pump LED to one of a shorter wavelength (Subtask 4.1). Three critical metrics for the assessment of a cyan-enhanced white-light LED device are Melanopic Daylight Efficacy Ratio (MDER), overall performance in Color Rendering Index (CRI), and Luminous Efficacy of Radiation (LER). We use the published standards CIE S 026-2018 for MDER and CIE 1938 for CRI. Because LER, MDER, and CRI have trade-offs with each other, it is non-trivial to hit a goal of MDER > 0.7—at least, not without potentially seriously degrading the other two metrics.

The effects of altering LED pump wavelength, cyan QD peak wavelength, and their relative amplitudes on MDER, CRI, and LER were modeled using custom software written in Igor Pro. Colleagues at Columbia shipped cyan InP/ZnS QDs to the Molecular Foundry for measurements at various concentrations at four different pump wavelengths: 395, 405, 425, and 450 nm. From the concentration series, we were able to determine the amount of red-shifting of the QDs as a result of self-absorption. The commercial Cd-based product from OSRAM was used as a basis spectrum (**Figure 25**).

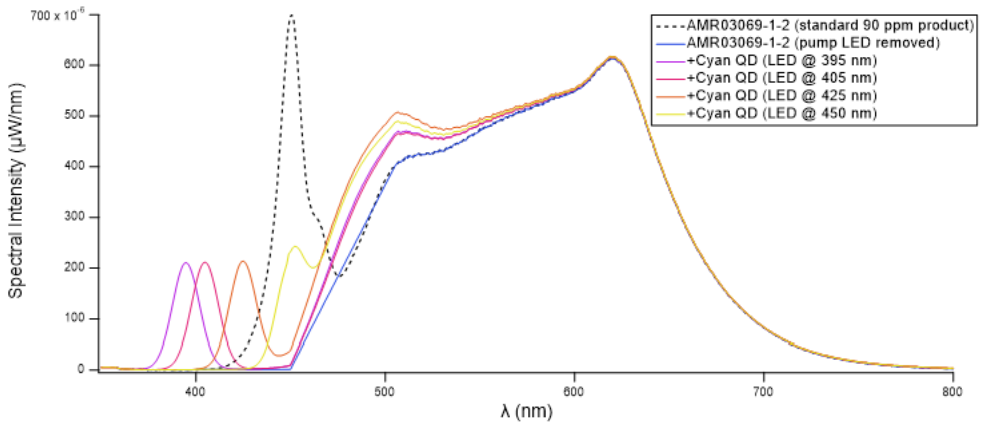

Figure 25. The black, dashed line is a spectrum which is representative of a typical 90 ppm white-light device. The darker blue spectrum is the 90 ppm white device spectrum without the contribution from the blue pump LED. The other four spectra are simulations, showing a selection at varying pump LED wavelengths (QD peak wavelength and both relative amplitudes are similar but not identical), demonstrating clear enhancements in the cyan region.

MDER, LER, and CRI values were calculated for each of the simulated spectra and placed into an array. A set of filter parameters were applied to the array, producing a truncated version containing only those entries which satisfy the color metric criteria. Through several simulation runs with increasingly narrower parameter bounds and higher granularity, the final run resulted in a total of 212,486 discreet spectra. Using the filtering rules below, 3,097 met the required criteria (**Figure 26**).

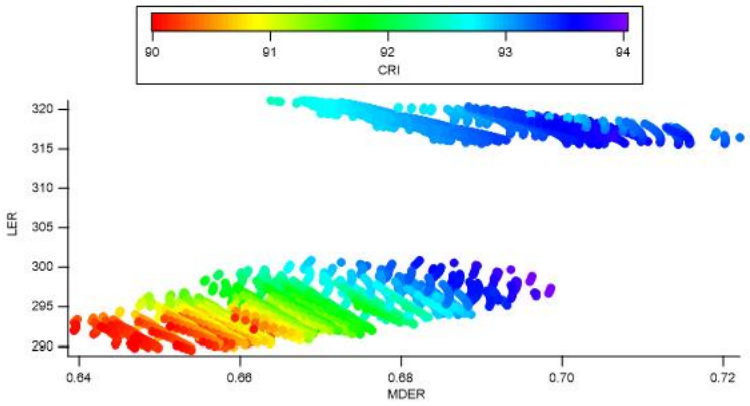

Figure 26. MDER, LER, and CRI (Ra) values for each of the 3,097 spectra which met the filtering criteria. The two distinct clusters were generated using the pump LED at 425 nm (lower left) and 450 nm (upper right).

From this dataset, we can make several observations. Importantly, only the pump LEDs at 425 and 450 nm were able to provide spectra which met the filtering requirements. When the pump LED is at 425 nm, CRI, LER, and MDER are all positively correlated. However, LER is always substantially lower for the 425 nm pump than the 450 nm pump. When the pump LED is 450 nm, higher MDER values tend to negatively correlate with LER. At the 450 nm pump, peak CRI (Ra) performance occurs at an MDER of 0.70. For the pump wavelengths of 395 and 405 nm, the CRI and R9 criteria were far from being met. From this simulation, a 450 nm pump LED was chosen for all devices in the project because it provides the optimal combination of metrics.

IIID.2 Barrier-Coated QD Stability on LED

The samples selected for on-chip reliability measurements were tested using a mid-power 2835 LED package. We tested the LEDs under four testing conditions, two of which were electrically driven. For the electrically driven conditions, we chose one Wet High Temperature Operating Lifetime (WHTOL) condition with a temperature of 85 °C, a Relative Humidity (RH)

of 85%, and a drive current of 40 mA. The other electrically driven condition was a High Temperature Operating Lifetime (HTOL) condition with a temperature of 85 °C, an ambient RH, and a drive current of 200 mA. The remaining two conditions were not electrically driven and are referred to as storage conditions. These storage conditions were a Wet High Temperature Non-Operating Lifetime (WHTNOL) condition with a temperature of 85 °C and a RH of 85%, and a High Temperature Non-Operating Lifetime (HTNOL) condition with a temperature of 85 °C and an ambient RH.

During Q6, materials were tested at a different temperature for the HTOL and HTNOL conditions. There were two HTNOL conditions: 65 °C/ambient RH and 115 °C/ambient RH, and the HTOL condition was run at 115 °C/ambient RH/200 mA drive current. The decision to alter the oven temperature in Q8 was made to simplify the comparison between WHTNOL/WHTOL and HTNOL/HTOL test conditions by having all conditions run at the same temperature. The reliability data that we present in this report includes data from Q6 to show the progression of our QD and barrier technology. The Q6 samples are identified as "Previous generation QDs".

Table 5. Description and PLQY of QD samples selected for reliability testing.

Source QD Type	Encapsulation	Sample form factor before processing for on-chip testing	PLQY before processing for on-chip testing	T_0 measurement, QDs in cured polymer on-chip
InP/ZnS	No	QDs in solution	46%	22%
InP/ZnS	Improved barrier coating	Dried QD powder	21%	23%

In **Figure 27**, we show the PLQY maintenance of our Cd-free QDs on chip for the WHTNOL condition, calculated by normalizing the PLQY values to the initial measurement of each sample. The green and purple traces represent the unencapsulated QDs and the barrier coated QDs given in **Table 5**. The red and blue traces show the materials that were tested in Q6. In this WHTNOL condition, both the unencapsulated and encapsulated QDs outperform the previous generation QDs, and the improved barrier coating provides further protection against the humidity present in the climate chamber. **Figure 28** shows the PLQY maintenance of QD materials under the WHTOL condition. This condition shows the impact of drive current on the QDs in a humid environment. The improved barrier chemistry in combination with our new generation QD shows increased stability under this condition, with 80% PLQY maintained after 4 hours, and >25% PLQY retention at 24 hours.

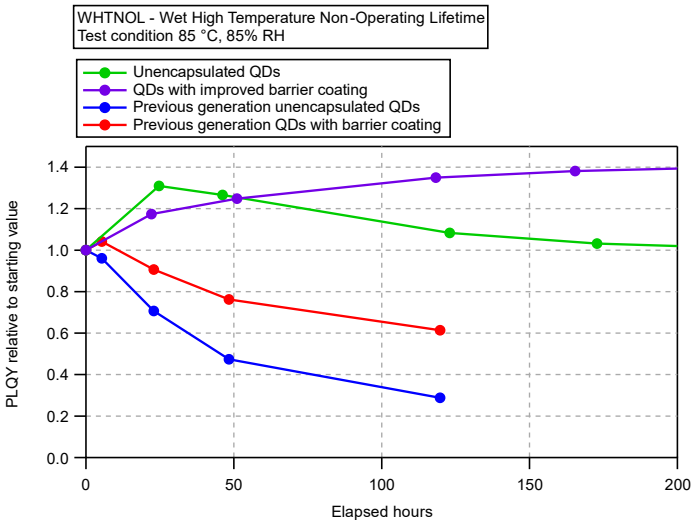

Figure 27. On-chip reliability testing data for WHTNOL condition.

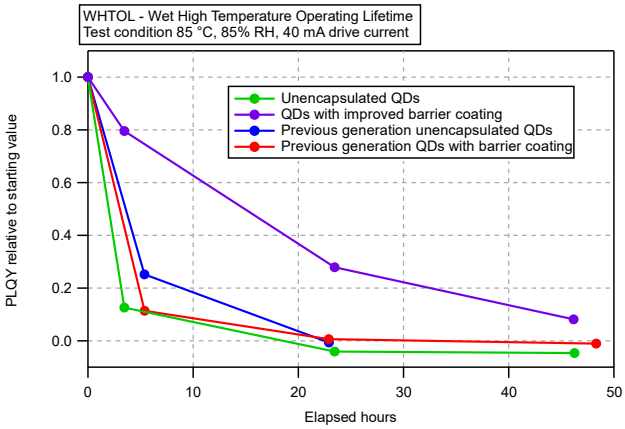

Figure 28. On-chip reliability testing data for WHTOL condition.

In **Figures 29 and 30**, we show the PLQY maintenance of the samples in HTNOL and HTOL test conditions. The dotted (**Figure 29**) and dashed (**Figures 29 and 30**) lines in red and blue indicate the testing temperatures that were used in Q6. The new generation of QDs and the improved barrier coating do not provide improvements to QD stability in the HTNOL and HTOL conditions when compared to the previous generation reported on in Q6.

QD stability on-chip is the primary roadblock toward realizing a down-converted, cyan-enhanced QD-LED. At the conclusion of this project, we have been unable to develop a suitable barrier coating that fully protects the QDs from degradation under high flux. We explored porous glass, metal phosphates, and adjustments in our proprietary barrier technology, all of which yielded valuable information that we can carry into future projects.

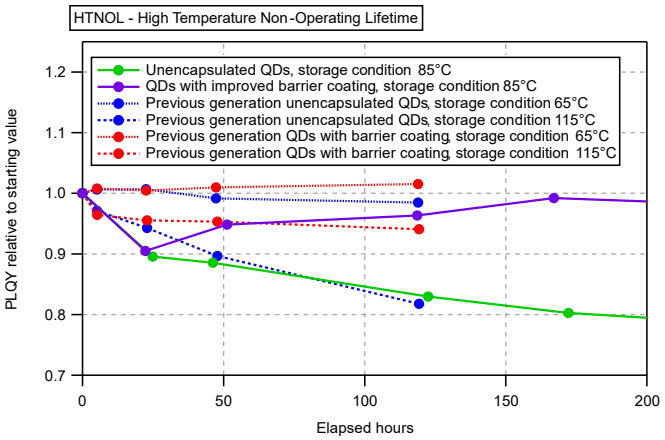

Figure 29. On-chip reliability testing data for HTNOL condition.

IIID.3 HCL Demonstration – CRI 95

At the conclusions of Year 1 and Year 2, we made demonstrator devices using the best-performing cyan- and red-emitting QDs within the wavelength ranges required to achieve the color temperature and MDER restrictions, highlighting the benefits of tunable, narrow emitters. The tasks were to demonstrate devices meeting CRI 95 or CRI 90 along with an MDER required for human centric lighting standards, ≥ 0.7.

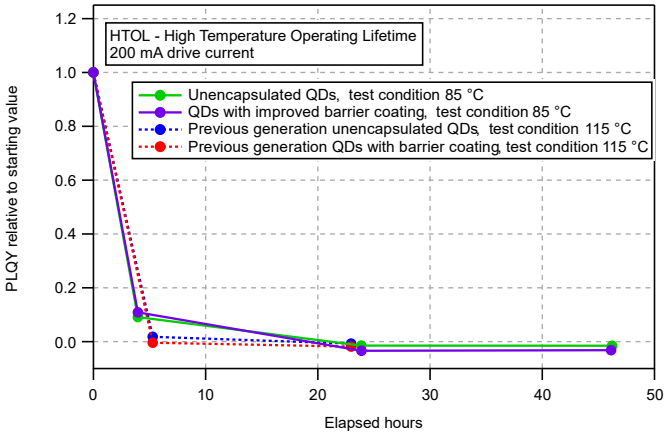

Figure 30. On-chip reliability testing data for HTOL condition.

First, the device targets for the CRI 95 device were to achieve a color of 4000K CCT, CRI $R_a \geq 95$ and MDER ≥ 0.7 by using both cyan QDs (to improve the MDER) and deep red QDs to help achieve a high CRI. To further fill in the spectral gaps between the cyan QD and red QD emission, we blended them with traditional broad band phosphors to better meet the CCT target. A comparison of the solution emission data for the two QDs used in the CRI 95 device is below in **Table 6**. The red QDs we used were InP/ZnSeS/ZnS with a high solution quantum yield of 85%

and a centroid of 631 nm. The cyan QDs were InP/ZnS with a solution quantum yield of 63% and centroid of 483 nm.

Table 6. Solution emission data for the cyan and red QDs used in the CRI95 device.

Solution Emission Data		
Color	Cyan	Red
PLQY	0.63	0.85
Centroid	483	631
Peak	479	626
FWHM	47	48

The device was prepared by mixing a slurry of quantum dots and phosphors in a phenyl methyl high refractive index silicone. The formulation was challenging to target the right color point while meeting all the required optical metrics. In the end, we used 4 total phosphors with the cyan and red QDs, for a total of 6 converters in the formulation. **Figure 31** shows the resulting prepared device spectrum measured at 25 °C at a current of 65 mA.

Table 7. Optical measurements from CRI 95 device.

25 °C Device Optical Data	CRI95 device with cyan + red Cd free QDs
Lumens	22.3
CCT	4170
CRI R_a	95
CRI R_9	84
LER	270.3
lm/W	126.6
MDER	0.70

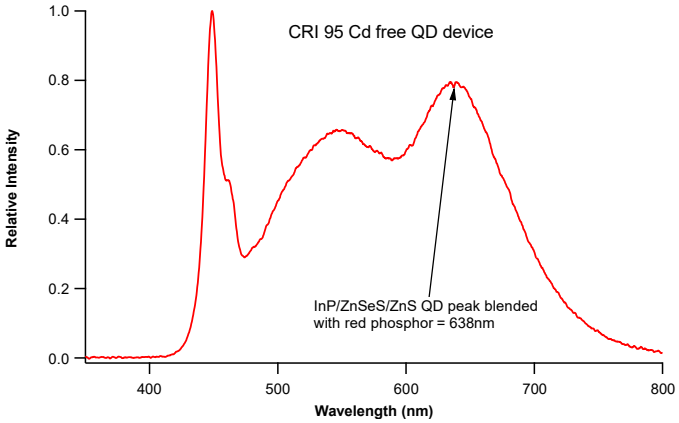

Figure 31. CRI 95 device spectrum measured at 25 °C at 65 mA.

The optical results in **Table 7** from the CRI 95 demonstrator device showed a very high CRI R_a of 95 along with quite high CRI R_9 of 84. We were pleased to see that the device with the small addition of the cyan QDs had an MDER of exactly 0.70, meeting the milestone target. Though not a specific requirement, the lm/W of the device measured 126.6, which is respectable for such a mid-powder high CRI device. Nichia's all phosphor Optisolis 757 mid-power device, which is also a CRI 95 product, has a 4000K CCT at a brightness of 138 lm/W. This further highlights the future need for tunable, narrow emitters for spectral engineering when looking at all the desired optical metrics.

IIID.4 HCL Demonstration – CRI 90

Throughout the duration of this project, we focused on the development of cyan-enhanced CRI 90 devices. First, we validated the benefit of a cyan QD emitter for use in a CRI 90 device by using the Cd-based materials available at the time. The addition of a cyan emitter in a 4000K CCT formulation increased the Melanopic Daylight Efficacy Ratio (MDER) above 0.7. A baseline cyan-enhanced HCL device was constructed using cyan ZnCdSSe/ZnS QDs from Columbia. We also used 90 ppm of Cd-containing ams-OSRAM red QDs (**Figure 32**). However, this required another deep red phosphor to achieve the target color rendering of CRI >90. The use of a broadband deep

red phosphor reduces the brightness potential of a device since there is less overlap with the photopic efficacy curve. The baseline device measured 124 lm/W with an MDER of 0.76 and an excellent CRI of 92 (**Table 8**).

Table 8. Performance for Cd-containing and Cd-free HCL devices.

Optical Metrics	Baseline Cd-containing Device	M4.3.1 Cd-free HCL Device	M4.3.3 Final Cd Free HCl Device	M4.3.3 Targets
Lumens	21.78	24.33	25.0	-
lm/W	123.5	138.5	**142.3**	**210✖**
LER	301	332	330	-
CCT	4030	4261	**4003**	**4000 ✓**
CRI	92	91	**92**	**> 90 ✓**
MDER	0.76	0.71	**0.70**	**> 0.7 ✓**

Our next step in the development progression was to only use Cd-free QDs in our devices—this was the task in Milestone 4.3.1. Since we were using Cd-free QDs without a RoHS restriction, we used more of the Cd-free QDs in the device formulation, thereby allowing for removal of our deep red phosphor and improving the device's brightness. The device for M4.3.1 measured at 138.5 lm/W, a 12% improvement over our baseline Cd-containing device but falling short of our 160 lm/W goal (**Table 8**). We hypothesized that increasing the PLQY of the QDs would improve the brightness in subsequent quarters.

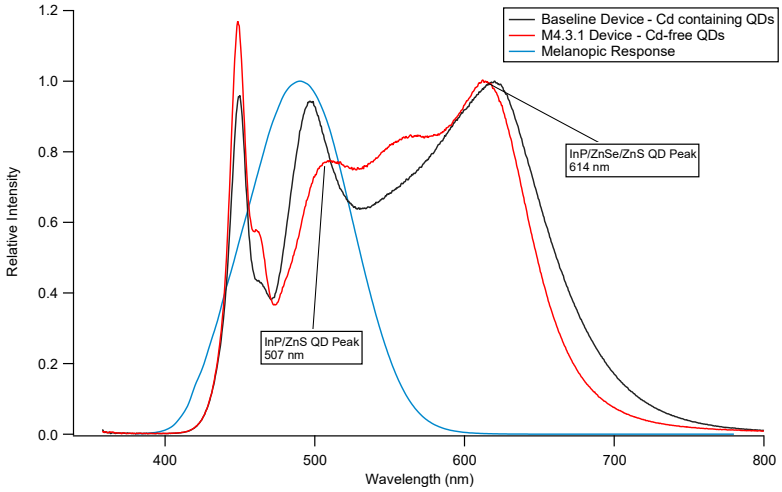

Figure 32. Spectrum of M4.3.1 device containing both cyan and red Cd-free QDs compared to the baseline HCL device under M4.1.1. Spectra are normalized to the red QD peak to show the reduction of the red emission tail.

The final device goal in Milestone 4.3.3 aimed toward achieving the highest device brightness of 210 lm/W while maintaining an MDER of ≥0.7. The 210 lm/W and CRI ≥90 metrics would match some of the very best mid-power LED performances currently on the market. Typically, these devices do not focus also on an MDER value. **Table 9** gives the solution emission data from the red and cyan QDs used towards the final device target. The red QD used in the M4.3.3 device was slightly redder by 3 nm compared to what was used in M4.3.1 device, but about 58% brighter with a PLQY of 77%. The cyan QD in this device had a PLQY of 63% vs 68% in the M4.3.1 device.

Table 9. Solution emission data for the cyan and red QDs used in the Cd-free CRI 90 devices.

Solution Emission Data					
Device	M4.3.1		M4.3.3		
QD Color	Cyan	Red	Cyan1 (Cd-free)	Cyan2 (low-Cd)	Red
PLQY	0.68	0.49	0.63	0.99	0.77
Centroid	488	617	478	478	620
Peak	485	613	477	477	616
FWHM	47	50	49	38	50

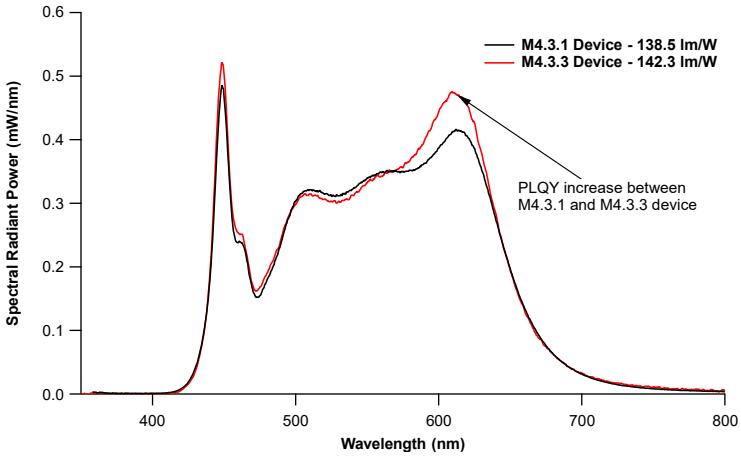

Figure 33. Spectral comparisons between M4.3.1 device and M4.3.3 device.

As can be seen in **Table 8,** the final milestone device measures below the target of 210 lm/W. However, it slightly improved over our M4.3.1 device—the device performance of 142.3 lm/W was a 2.7% increase over the M4.3.1 device, but still only 67% of the final M4.3.3 target. In **Figure 33** we show the spectral changes to M4.3.3 over M4.3.1. Clearly, the improvement in the red QD PLQY used in the M4.3.3 device led to an increase in the red watts and helped increase the device brightness for the same CCT. Still, the device fell short of the 210 lm/W target. We hypothesized that some portion of the cyan QDs was exciting the other phosphors along with the red QDs. This double pumping loss pathway happens in typical all-phosphor LED formulations where there is a green and red emitting phosphor. For example, a portion of the emission from the green phosphor excites the red phosphor and this process leads to overall system efficiency decreases. While the cyan QDs help meet the MDER target of 0.7, they may also be contributing towards overall device brightness decreases.

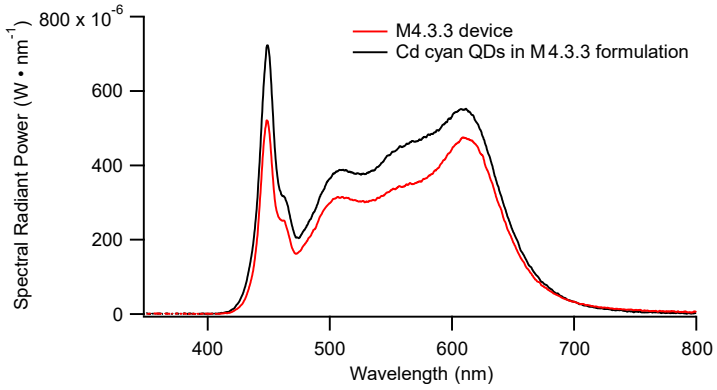

Figure 34. Spectral comparison for the Cd-free and low-Cd M4.3.3 devices.

To test whether double pumping was a major contributing loss pathway, we utilized our final no-cost extension to demonstrate the importance of high QYs for all the emitters, but particularly for the cyan QD. We swapped a low-Cd cyan QD into the same phosphor + QD formulation used in the M4.3.3 device. The solution emission metrics of the brighter, low-Cd cyan QD are

given in **Table 9**. The similarity of the two centroid and peak values makes it possible to compare only the difference in PLQY when used in a device. As can be seen in **Figure 34**, the resulting device spectrum increased in brightness and gave a value of 178.5 lm/W, 25% brighter than the M4.3.3 result. Importantly, lighting metrics remained mostly unchanged (**Table 10**).

Table 10. Performance for low-Cd and Cd-free HCL devices vs ams-OSRAM commercial HCL device.

Optical Metrics	M4.3.3 final Cd-free device	M4.3.3 formulation w/ low-Cd cyan QD	OSCONIQ® E 2835 Cyan Enhanced	Final Project Targets
lm/W	142.3	178.5	157	**210**
LER	330	332	327	**-**
CCT	4003	4260	4000	**4000**
CRI	92	89	83	**≥ 90**
MDER	0.70	0.71	0.71	**≥ 0.7**

The latest device results are particularly noteworthy, as the device with low-Cd cyan QDs outperforms our own commercial HCL device while achieving an improved CRI. In **Table 10**, we compare our Osconiq 2835 cyan-enhanced LED (a 2-chip device with 450 and 475 nm LEDs) to our formulation with all high QY emitters. The 2-chip cyan-enhanced LED has limitations, primarily stemming from its lower wall plug efficiency due to the dual chip design. Consequently, this impacts the overall device brightness that can be attained. A more straightforward design approach involves using a single, highly efficient 450 nm LED, coupled with high QY converters to spectrally engineer the formulation for the desired performance metrics. Our latest device exemplifies this approach, utilizing low-Cd high QY cyan QDs formulated with phosphors and our Cd-free red QDs.

IV. Final Outlook

We have shown that bright low-Cd cyan QDs can enable human centric lighting with performance on par with products on the market. Obtaining high-quality InP-based cyan emitters remains challenging due to their propensity to form surface defects, a consequence of their high surface-to-volume ratio. Complete confinement of the exciton with epitaxial, crystalline, and lattice-matched shell deposition is crucial for any color of InP-based core/shell/shell heterostructure for preventing flux-induced degradation. An abundance of barrier and encapsulation technologies remains to be explored toward protecting the QDs from loss pathways on-chip. Stability continues to be the primary obstacle toward widespread adoption of Cd-free QDs in high efficacy solid state lighting products.